Structure

Article

Lipids modulate the open probability of RyR1 under cryo-EM conditions

Graphical abstract

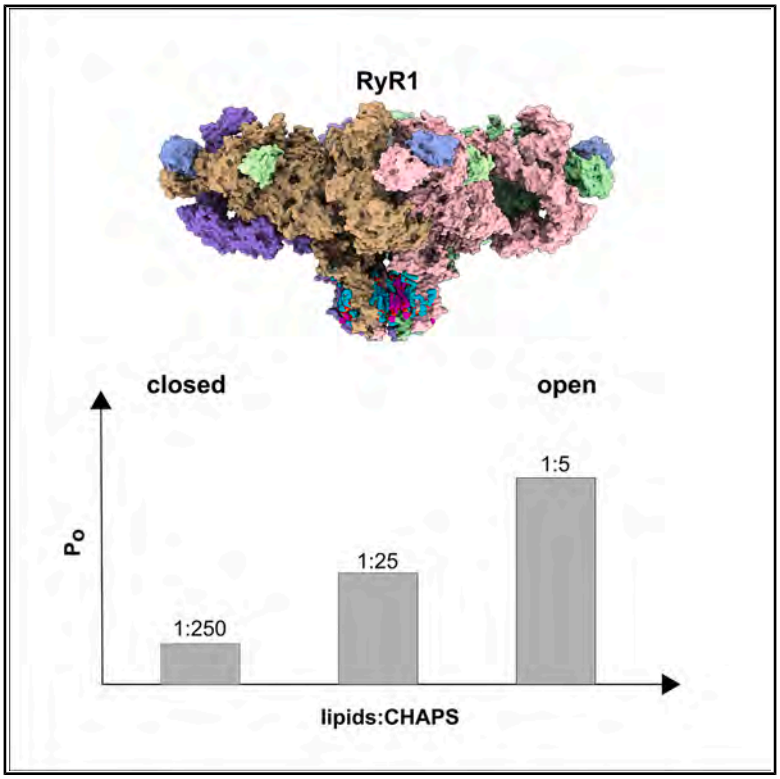

Highlights

- Most RyR1 particles are trapped in the open conformation when 0.05% POPC is added
- Two layers of ordered lipids are resolved around RyR1
- MSP1E3D nanodiscs prevent RyR1 from opening in response to common activators

Authors

Chenyao Li (李陈瑶), Rouslan G. Efremov

Correspondence

rouslan.efremov@vub.be

In brief

Chenyao Li et al. using single particle cryogenic electron microscopy show that in detergent-solubilized ion channel RyR1, the channel switching between open and closed states can be modulated by adding lipids to the detergent solution. Multiple ordered lipid molecules interacting with RyR1 were modeled.

Li & Efremov, 2025, Structure *33*, 1–12
December 4, 2025
https://doi.org/10.1016/j.str.2025.09.003

CellPress

Please cite this article in press as: Li and Efremov, Lipids modulate the open probability of RyR1 under cryo-EM conditions, Structure (2025), https://doi.org/10.1016/j.str.2025.09.003

Structure

CellPress

Article

Lipids modulate the open probability of RyR1 under cryo-EM conditions

Chenyao Li (李陈瑶)[1,2,3] and Rouslan G. Efremov[1,2,4,*]
[1]Center for Structural Biology, Vlaams Instituut voor Biotechnologie, 1050 Brussels, Belgium
[2]Structural Biology Brussels, Department of Bioengineering Sciences, VUB, 1050 Brussels, Belgium
[3]Present address: Hangzhou Institute of Medicine, Chinese Academy of Sciences
[4]Lead contact
*Correspondence: rouslan.efremov@vub.be
https://doi.org/10.1016/j.str.2025.09.003

SUMMARY

Ryanodine receptors (RyRs) are intracellular tetrameric ion channels responsible for Ca^{2+} release from the sarcoplasmic and endoplasmic reticulum. Ryanodine receptor 1 (RyR1) isoform, critical for muscle contraction, has been studied most extensively. While cryoelectron microscopy (cryo-EM) has been instrumental in revealing near-atomic details of RyR gating mechanisms, the open probability of RyR1 under cryo-EM conditions is notably lower than that observed in electrophysiological studies. Here, we present a cryo-EM study examining the open probability of RyR1 solubilized in CHAPS with varying lipid concentrations. We found that increasing lipid concentration from 0.001% to 0.05% raised the RyR1 open probability from 16% to 84%, whereas RyR1 reconstituted into lipid nanodiscs remained closed. We modeled 72 lipid molecules in the map reconstructed at the highest lipid concentration. These findings demonstrate the important role of lipids in modulating the open fraction of solubilized RyR1 channels under cryo-EM conditions and suggest optimal lipid mimetics for structural studies of RyR1 gating.

INTRODUCTION

Structural studies of ion channels are often performed on the detergent-solubilized proteins.[1–4] Alternative systems include lipid nanodiscs, amphipols, and, more recently, lipid liposomes and native membranes.[5–11] Typically, structural studies aim at determining the structures of ion channels in several functional conformations, such as closed, open, deactivated, or primed states.[3,12,13] However, the physiological function of ion channels also involves fine regulation of their open probability, which is modulated by interactions with soluble or membrane-embedded molecules or by changes in lipid membrane state, including transmembrane electrochemical potential and lipid composition.[14–16] Such modulation can be studied using single-particle cryoelectron microscopy (cryo-EM), which, in addition to resolving structures of functional conformations, provides particle counts for each conformation. From these counts, the relative occupancies of the conformations can be determined. Thereby, the contribution of individual factors, such as binding of small molecules and proteins, post-translational modifications, temperature, and pH to channel gating can be studied. However, the distribution of channel conformations is also modulated by lipids and lipid mimetics in a channel-specific manner,[17–21] often not well characterized.

The ryanodine receptors (RyRs) are homo tetrameric Ca^{2+} channels with a molecular weight of around 2.2 MDa.[22,23] They reside in the sarcoplasmic or endoplasmic reticulum (SR/ER) membrane where they mediate calcium release in an isoform-dependent manner.[22,24,25] Among three RyR isoforms found in mammals, RyR1 is primarily expressed in skeletal muscles, RyR2 in the heart, and RyR3 is expressed at low levels in various tissues.[22,26]

RyR1 plays a crucial role in excitation-contraction coupling by releasing Ca^{2+} from SR to cytoplasm, triggering muscle contraction.[27,28] Hence, precise control of RyR1 gating is essential for normal physiological function, whereas Ca^{2+} leakage can lead to diseases such as malignant hyperthermia and central core disease (CCD).[29,30] Because even subtle changes in RyR1 gating lead to disease, understanding how individual factors, including membrane mimetics, fine-tune the open probability of RyR1 is essential.

While much research has been conducted on regulatory mechanisms of binder proteins and small molecules,[13,31–36] fewer studies have explored how membrane mimetics used to study RyR1 regulation by cryo-EM influence RyR1 open probability.[18,34]

Previous studies have observed that the open probability of RyR1 derived from analysis of single particle cryo-EM data of detergent-solubilized RyR1 (~50%) was about twice as low as the nearly 100% open probability observed in single-channel recordings under otherwise identical conditions.[13] Curiously, the open probability of RyR1 reconstituted into liposomes estimated by cryo-EM was still low (37% and 62%).[34,37] Our previous study using H^3-ryanodine binding assays indicated that a

Please cite this article in press as: Li and Efremov, Lipids modulate the open probability of RyR1 under cryo-EM conditions, Structure (2025), https://doi.org/10.1016/j.str.2025.09.003

mixture of detergent 3-[(3-Cholamidopropyl)dimethylammonio]-1-propanesulfonate (CHAPS) with lipids at various concentrations tunes the open probability of detergent-solubilized RyR1.[18] However, this observation has not been verified using structural data, and the origin of such a modulation remains unclear.

To further understand the modulation of the open probability of RyR1 by lipid mimetics, we investigated the influence of lipids on the open fraction of detergent-solubilized RyR1 using cryo-EM. Here, we show that changing the amount of lipids added to detergent-solubilized RyR1 modulates the open fraction of RyR1 determined by cryo-EM between 16% and 84%. The reconstructions obtained at high lipid concentration allowed us to model 18 lipid molecules per RyR1 protomer and visualize the details of RyR1-lipid interactions. Structural analysis suggests that lipids modulate gating by establishing a hydrophobic barrier between the transmembrane domain and the hydrophilic buffer. These results indicate that the lipid concentration in the detergent micelles is a critical determinant of the channel open fraction and must be thoroughly controlled in the experiments seeking to study modulation of RyR1.

RESULTS

RyR1 structures with high concentrations of lipids

Previous cryo-EM studies of CHAPS-solubilized RyR1 utilized 0.001% of 1,2-dioleoyl-sn-glycero-3-phosphocholine (DOPC) or 1-palmitoyl-2-oleoyl-sn-glycero-3-phosphocholine (POPC) lipids in buffer containing 0.2%–0.25% CHAPS.[13,37] The RyR1's open probability under these conditions, estimated from the number of particles assigned to open and primed conformations, was between 16%[37] and 50%.[13] Our previous biochemical studies indicated that the open probability of solubilized RyR1 depends on the concentration of lipids.[18] To understand how the amount of lipids in the solubilized protein influences the structure and open probability of RyR1, we solved cryo-EM structures of the protein purified using RyR-specific nanobody Nb9657.[37] We plunged it in a buffer containing 0.2% CHAPS and either 10- or 50-fold higher concentration of POPC (0.01% and 0.05%, respectively). We note that the plunging protocol used in the study involved adding 1 mL of buffer without detergent and lipids on the back side of the grid, which introduced a 20% uncertainty in the final lipid concentration, corresponding to a 0.008%–0.01% range for the first and 0.04%–0.05% for the second dataset. The cryo-EM datasets were collected with 50 μM free Ca^{2+}, 2 mM ATP, and 5 mM caffeine—conditions that stabilize the open state of RyR1 with Po of 0.93 in single-channel electrophysiological recordings in PC:PE 5:3 membranes.[13] The elevated lipid concentration reduced the contrast of RyR1 particles in cryo-EM micrographs, with the 0.05% POPC dataset exhibiting a more pronounced contrast loss (Figures 1A and 1B). Nonetheless, after collecting around 3 times more micrographs, reconstructions of primed and open states were determined to a resolution between 3.3 and 3.6 Å for both datasets (Figures 1 and S1–S3; Table 1), which are further referred to as DT-0.05-primed, DT-0.05-open, DT-0.01-primed, and DT-0.01-open. Here, DT indicates that the protein was solubilized in detergent. Bound Nb9657 and endogenous co-purified FK506-binding protein 12 (FKBP12) were well resolved in the density maps (Figure 1E). Both datasets were processed using the same protocol, and the open probability estimated from the number of particles assigned to primed and open states was 67% for DT-0.01 and 84% for DT-0.05.

Lipids modulate the fraction of open RyR1

Two new datasets complement previously reported structures determined with 0.001% POPC (DT-0.001 dataset), reconstituted into lipid nanodiscs (ND dataset) and in POPC liposomes (LP dataset).[37] These 5 datasets were collected with RyR1 purified following the same purification protocol, using the same batch of membranes and the same stocks of detergent and lipids. The channel was stabilized in the open state using the same combination of channel activators, and the cryo-EM data were processed following the identical protocols.

In all our RyR1 preparations, endogenous (FKBP12) was co-purified, and Nb9657 was bound to the RY12 domain. FKBP12 reduces RyR1 dynamics and stabilizes the closed conformation of the channel.[39] Although the Nb9657 binding cleft on the RY12 domain is located distally from the pore, it is also emerging as an allosteric site.[35,36] To account for potential differences in the open fractions of RyR1 due to variations in the amounts of bound FKBP12 and Nb9659, their occupancies were analyzed using OccuPy program[40] (Figure S4) and by 3D classification focused on FKBP12 (Figure S5; Table S1). FKBP12 occupancy for CHAPS-solubilized datasets was in the range 20%–40% and 40%–50% for the ND and LP datasets, respectively. The 3D classification did not reveal a stark difference in FKBP occupancies between the open and closed states, suggesting a limited effect of FKBP on the open-closed equilibrium under our experimental conditions. The Nb9657 occupancy closely matched that of the flexible RY12 domain (suggesting a stoichiometric complex). Since the only experimental variable between datasets was the type of lipid mimetic used, the observed differences in RyR1 open-state fractions can be attributable to the lipid mimetics.

The fraction of open RyR1 solubilized in CHAPS was strongly modulated by lipids. It increased from 16 to 67 and to 84% as lipid concentration grew from 0.001 to 0.01 and 0.05% POPC, respectively (Figure 2; Table S2). Unexpectedly, for RyR1 reconstituted into lipid nanodiscs, 3D classification consistently failed to identify the open conformation, suggesting that RyR1 remained fully closed. In contrast, the open fraction of RyR1 reconstituted into lipid liposomes (62%)[37] was lower than that of DT-0.01 (67%) and DT-0.05 (84%).

Previous reports have documented the influence of lipid mimetics on protein conformations.[20,41] To verify if similar effects can be observed for RyR1, we compared its pore profile for the structures determined with different mimetics (Figure S6). The overall RyR1 structures and pore profiles of the primed and open states did not show strong dependence on lipid mimetics. However, small systematic variations in the channel width (the amplitude of 1–1.5 Å for the Cα-Cα distance of gate residues I4937) were observed (Figures S6C and S6D). The gate appears to be tighter in the structures with a low and wider with a higher population of open state. However, small amplitude and possible contribution of imperfection in 3D classification due to the large differences in the fractions of open and closed conformations between the datasets leave their interpretation ambiguous.

Please cite this article in press as: Li and Efremov, Lipids modulate the open probability of RyR1 under cryo-EM conditions, Structure (2025), https://doi.org/10.1016/j.str.2025.09.003

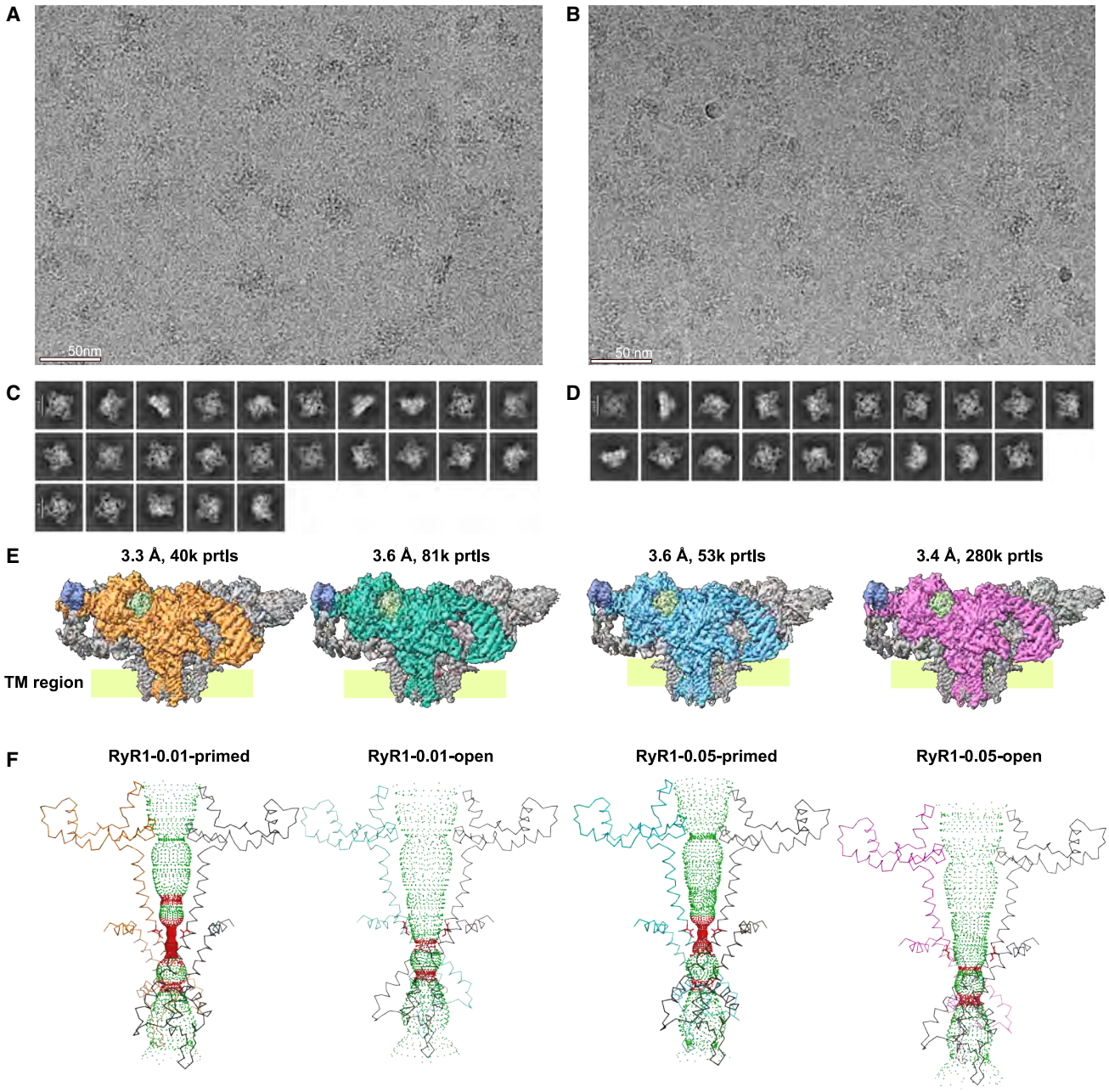

Figure 1. Cryo-EM structures of RyR1 with 0.01 and 0.05% POPC

(A and B) Cryo-EM micrographs for the datasets with 0.01% and 0.05% POPC, respectively, the scale bars are 50 nm.

(C and D) Corresponding 2D class averages. The scale bars are 200 Å (C) and 210 Å (D).

(E) 3D density maps of the structures determined from the two datasets, from left to right: DT-0.01-primed, DT-0.01-open, DT-0.05-primed, and DT-0.05-open. The nanobody is shown in blue, FKBP12 in light green, and one monomer from each structure is colored orange, spring green, cyan, and magenta, respectively.

(F) Side view of the pore region for each structure showing two protomers—one in gray and the other colored as in (E). The gate residue, I4937, is highlighted in red. The solvent-accessible surface of the channel, calculated using HOLE,[38] is shown in green for channel regions with a radius above 4 Å and in red for those below 4 Å.

See also Figures S1–S3.

Belt of ordered annular lipids is resolved at high lipid concentration

The map of DT-0.05-open resolved multiple elongated densities into which 72 lipids (18 per protomer named L0-L17) were modeled (Figures 3 and 4). This is an improvement in comparison to the published RyR structures, with typically only two lipids modeled per protomer,[43] and seven lipids in the closely related IP3R channel.[12] At the same time, no density for ordered

Please cite this article in press as: Li and Efremov, Lipids modulate the open probability of RyR1 under cryo-EM conditions, Structure (2025), https://doi.org/10.1016/j.str.2025.09.003

Table 1. Statistics of cryo-EM data and models

Sample	0.05% lipids		0.01% lipids	
State	open	primed	open	primed
Ligands	50μM free Ca^{2+}, 2mM ATP, 5mM caffeine			
PDB ID	9HEO	9R8O	9HEQ	9RCW
EMBD ID	EMD-52085	EMD-53834	EMD-52091	EMD-53924
Data collection				
Microscope	JOEL CRYOARM300			
Detector	Gatan K3			
Voltage (kV)	300			
Magnification	60,000			
Exposure time (S)	2,796			
Electro dose (e −/Å^2)	60			
Number of frames	60			
Defocus range (μm)	1.5–2.5			
Pixel size (Å)	0.713		0.727	
Symmetry	C4			
Collected images	22,931		7,480	
Used images	12,534		5,840	
Final particles (N)	279,776	53,158	80,709	39,983
Global map resolution (Å)	3.4	3.6	3.6	3.3
Local maps resolution range (Å)	3.3–3.6	3.3–4.4	3.1–3.9	3.0–3.8
Model refinement				
Refinement package	Phenix v 1.20.1			
Initial model used	–		–	
Model resolution [Å^2], FSC = 0.5	3.3	3.6	3.6	3.7
Model composition				
Non-hydrogen protein atoms	146,795	145,532	145,448	144,636
Protein residues	18,240	18,224	18,208	18,204
Ligands	88	56	56	40
B-factors mean [Å^2]				
Protein	122.60	111.24	133.08	151.62
Ligand	112.87	110.75	142.02	85.74
R.M.S deviations				
Bond lengths (Å)	0.004	0.003	0.004	0.005
Bond angles (°)	0.909	0.773	0.814	0.831
Validation				
Molprobity score	1.78	1.64	1.63	1.74
Clashscore	11.73	10.31	10	10.87
Poor rotamers (%)	0.44	0.59	0.70	0.83
Ramachandran plot				
Favored (%)	96.84	97.45	97.47	96.89
Allowed (%)	3.14	2.50	2.44	3.11
Disallowed (%)	0.02	0.04	0.09	0.00

CHAPS molecules, which are steroid derivatives featuring flat structures composed of four fused rings easily distinguishable from phospholipids, was observed despite high CHAPS concentration (molar ratios CHAPS:lipids were in the range 250:1–5:1). Even though DT-0.05-open map had lower resolution than the maps solved at lower lipid concentrations (DT-0.001-primed or ND-primed), the lipid densities were better defined and had unambiguous connectivity (Figure 4; Video S1). The lipids, modeled as POPC according to the lipid added during the protein preparation, cover nearly completely the concave regions of the *trans*-membrane domain formed between the 4-helical voltage sensor-like helical bundles (S1–S4) (Figure 3).

Please cite this article in press as: Li and Efremov, Lipids modulate the open probability of RyR1 under cryo-EM conditions, Structure (2025), https://doi.org/10.1016/j.str.2025.09.003

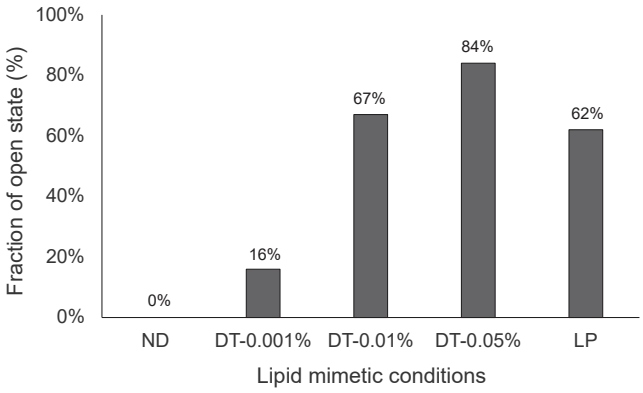

Figure 2. Fraction of open RyR1 in different lipid mimetics

The open fractions of RyR1 were calculated by counting the number of particles assigned to the open conformation relative to the total particle count in the high-resolution maps (Table S1). From left to right, ND: RyR1 in nanodiscs, DT: RyR1 in CHAPS micelles supplemented with POPC at indicated concentrations, and LP: RyR1 reconstituted into POPC liposomes.

ND and LP datasets are from a study by Li et al.[37] See also Tables S1 and S2; Figures S4–S6.

The modeled lipids are organized in two layers around the surface of the membrane-embedded RyR1 region. The annular layer of lipids interacts directly with RyR1 (Figures 3, 4A, and 4B) and accounts for 13 lipids and lipid fragments. Among the lipids with modeled head groups, 3 are located on the luminal (Figures 3A and 3C) and 9 on the cytoplasmic leaflet. The second layer of lipids comprises 5 lipids and lipid fragments that fill the concave surface of the *trans*-membrane domain with 3 cytoplasmic and 2 luminal lipids (magenta in Figures 3 and 4).

The lipid interactions with RyR1 were analyzed using the protein-ligand interaction profiler.[42] In total, 49 residues per protomer interact with lipids (Figure 4); all are conserved between rabbit and human RyR1. The annular lipids interact extensively with the protein via hydrophobic interactions and several putative polar contacts with amino acid residues located at the interface between hydrophobic and polar surfaces of the transmembrane domain (Figure S7). Lipids from the second layer, on the other hand, interact only with annular lipids except for L3 and L15 that may form a hydrogen bond with Y4912 and N4787, respectively (Figure 4B). Among the residues interacting with lipids, mutations R4824C (R4825 in humans), A4845V (A4846 in humans), and F4859 deletion (F4860 in humans) have been associated with CCD, whereas the mutation A4845V was linked to myotonic dystrophy type 1[44,45] (Figure S7).

To understand the role of lipids in stabilizing the open RyR1 conformation, we compared the density of lipids between the maps obtained from detergent-solubilized RyR1 prepared with different lipid concentrations and RyR1 reconstituted into nanodiscs and liposomes. For this, we computed the correlation coefficient between the map and lipid model (only maps resolved to better than 4.0 Å were considered) (Figure S8). The DT-0.05-open map had the best resolved lipid densities. At lower lipid concentrations, densities for five annular lipids (L0, L1, L6, L9, and L14) were well resolved, four other lipids (L5, L12, L8, and L16) were completely absent, while remaining lipid densities were weaker and fragmented, but their positions were unchanged. The densities for the second-layer lipids were weak in the DT-0.05-open map and not resolved at lower lipid concentrations. This suggests that increasing lipid concentration leads to populating lipids in the weaker binding sites around the *trans*-membrane domain, forming a lipid-bilayer-like structure between the S1-S4 lobes. Surprisingly, lipid densities in ND-primed and RyR1 primed state reconstruction determined by Melville et al.[34] were weak and comparable to the lipids in the DT-0.001-primed map (Figure S8), including five better-resolved lipids. This may stem from either reduced lipid dynamics in CHAPS micelles or higher lipid bilayer perturbation in nanodiscs and curved liposomes.

Structural adaptation of lipids upon the primed-to-open transition

The conformational changes in RyR1 transmembrane domain during transition from primed to open state include a ~2-degree outwards rotation of S1-S4 lobes and expansion of the cytoplasmic side of pore-forming S5-S6 helices with an amplitude of around 3 Å (Video S2). To understand the involvement of lipids in this transition and their possible role in stabilizing the open state conformation, we compared the RyR1-lipid interactions between the DT-0.05-open state and DT-0.05-primed states. Most of the resolved lipids and protein-lipid interactions are conserved between these states (Figure 5A). Only minor structural rearrangements in lipids L2, L7, L16, and L17 were observed. The lipid positions adapt to the altered membrane-exposed surface of the transmembrane domain without major changes in the protein-lipid interaction pattern (Figure 5B; Video S2).

Fraction of open channels correlates with the dimensions of the bilayer-mimicking belt

An additional insight into the properties of lipid bilayer mimetics was obtained from the analysis of the shape of the belt observed in the cryo-EM maps around the membrane domain of RyR1. This hydrophobic belt originates from the lipid bilayer mimetics and reflects its geometry. We compared the sizes of the nanodiscs, micelles, and liposomes for nine density maps (Figure 6A). The maps were low-pass filtered to a resolution of 8 Å, and the density levels were set to enclose identical volumes of the cytoplasmic domains of the RyR1 reconstructions.

The nanodisc belt had the smallest diameter of 142 Å (average value of three measurements; other diameters were calculated in the same way). For detergent-solubilized RyR1, the micelle sizes increased with lipid concentration from ~149 Å at 0.001% to 159 Å at 0.05% POPC, respectively. The density of liposome-reconstituted RyR1 had a diameter of ~156 Å (Figure 6) and reflected a geometrically consistent region of liposomes around the transmembrane domain.

In the open state, the size of the micelle increased by 6 ± 4 Å in accord with the outward rotation of the voltage-sensor-like lobes (the diameter of the modeled *trans*-membrane domain increased by ~5 Å from 131 to 136 Å). As lipid concentration increased, the grooves between S1-S4 lobes were less pronounced, and the overall shape of the micelle became rounder (Figure 6A), consistent with the binding of lipids in the grooves between S1-S4 lobes. Taken together, these data indicate that the fraction of

Please cite this article in press as: Li and Efremov, Lipids modulate the open probability of RyR1 under cryo-EM conditions, Structure (2025), https://doi.org/10.1016/j.str.2025.09.003

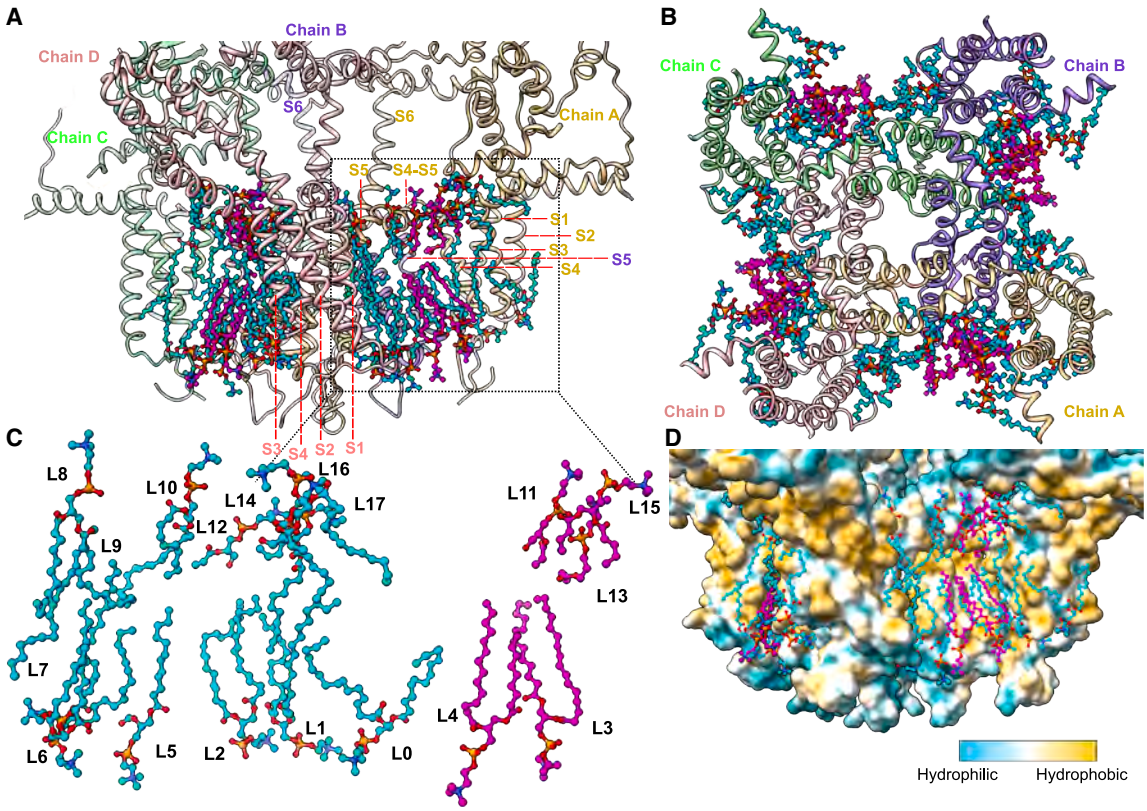

Figure 3. Lipids modeled in the RyR1 structure

(A and B) Side and top views of the POPC modeled into the DT-0.05-open map. The annular layer lipids are colored in cyan and the second-layer lipids in magenta. The RyR1 structure is presented as a cartoon and lipids are shown in ball-and-stick representation.

(C) An enlarged view of the modeled lipids. The second layer (right) is separated from the first (left) for better visualization.

(D) Lipid positions relative to RyR1 surface colored by hydrophobicity.

See also Figures S7 and S8.

open RyR1 particles correlates with the size of the belt, mimicking lipid bilayer. The size of the belt in LP datasets is likely less representative due to the continuous and strongly curved geometry of the liposomes.

DISCUSSION

Gating of the ion channel is a stochastic process; thus, even in the closed state, RyR1 shows rare transient spikes of conductivity.[13,46] Channel activators modulate the frequency of conductivity spikes and their length.[47] Cryo-EM captures statistically averaged conformations, which are expected to reflect the time-averages of open and closed channel states measured by single-channel electrophysiology. There is an agreement between electrophysiology and cryo-EM regarding the existence of two principal channel conductivity states: closed pore conformation that allows no current flow, and open pore conformation in which the hydrophobic gate formed by side chains of I4937 is open to a well-defined diameter that facilitates ion flow with a certain resistance. Where cryo-EM data consistently disagree with electrophysiology for RyR1 is the estimates of channel open probability, which is lower when estimated from cryo-EM data than observed in single-channel recordings. The underlying reasons for this discrepancy remain unknown.

In this work, using cryo-EM, we determined the open fractions of RyR1 solubilized in CHAPS with added 0.01% and 0.05% of POPC, which complements three other datasets: one with 0.001% POPC, one reconstituted into lipid nanodiscs, and another into POPC liposomes.

All RyR1 preparations used in this study were complexed with Nb9657, which binds to and alters the conformation of the RY12 domain at the periphery of the 270 Å cytoplasmic crown.[37] Recent studies suggested that, despite its remote location from the gate, the RY12 domain is an allosteric site.[35,36] Additionally, sub-stoichiometric occupancy of endogenous co-purified FKBP12 may influence the fraction of the open conformation.[39] Density analysis shows that Nb9657 and FKBP12 were bound with comparable occupancies across the five lipid mimetics discussed in this work, except for the ND and LP datasets, which had 10%–20% higher FKBP12 occupancy.

An example of lipid bilayer mimetics' effect on the opening of RyR1 has been documented: solubilized in Tween 20, RyR1 can be purified in a stable form, but the channel remains closed in the presence of activators.[48] Here, we show that for RyR1 solubilized in CHAPS, the open channel fraction is modulated by lipids

Please cite this article in press as: Li and Efremov, Lipids modulate the open probability of RyR1 under cryo-EM conditions, Structure (2025), https://doi.org/10.1016/j.str.2025.09.003

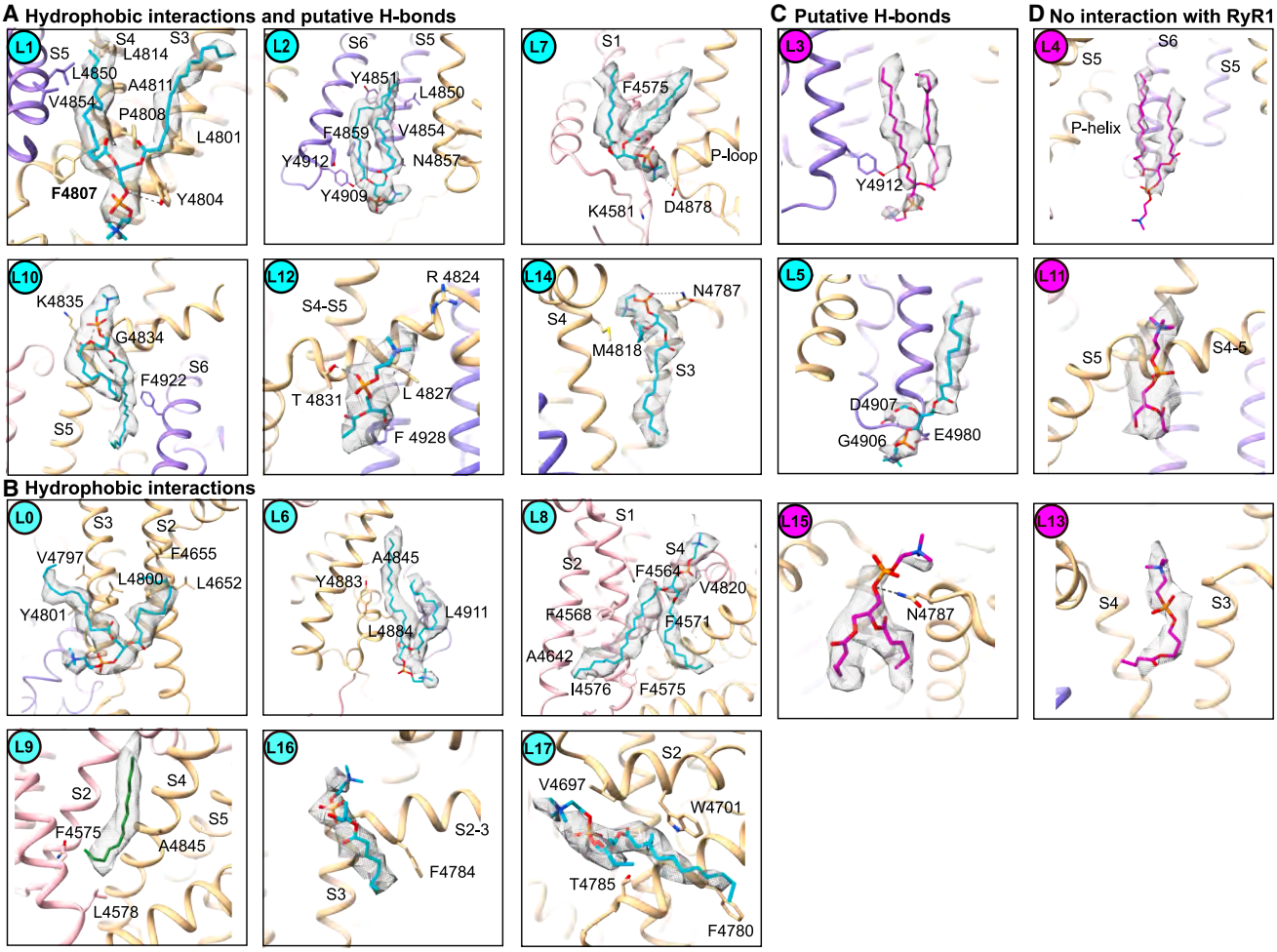

Figure 4. Details of RyR1-lipid interactions

Panels show the interaction of individual lipids with RyR1 and lipid densities. Lipids are grouped according to the type of interactions with the protein: (A) hydrophobic and putative hydrogen bonds, (B) hydrophobic interactions only, (C) putative hydrogen bonds only, and (D) lipids that do not interact with the protein. The interactions were analyzed using the PLIP web service.[42] The interacting residues are shown as sticks. The lipid number is indicated in the top left corner, and the color code is as in Figure 3. The lipid densities, displayed as gray mesh, were visualized in ChimeraX v1.9 using the surface zone command with a carving radius of 3.5 Å. The densities of neighboring lipids or residues within 3.5 Å were manually removed with Map Eraser, and a density threshold between 0.3 and 0.52 was applied.

See also Figure S8.

in a broad range under otherwise identical conditions. When lipid concentration was varied 50-fold between 0.001% and 0.05%, the fraction of open RyR1 increased from 16% to 84%. In this range, the CHAPS:POPC molar ratio changes from 250:1 to 5:1, such that the starting point represents nearly pure CHAPS micelles, whereas at high lipid concentration, about 20% of the molecules in a detergent micelle are POPC. The addition of lipids to detergent solution reduces the contrast of protein particles in the electron micrographs, and, therefore, is usually avoided during preparations of cryo-EM grids. As we show in this study, it might be desirable in specific cases, such as the studies of the open conformation of RyR1.

Two observations provided insights into possible mechanisms by which lipids shift the primed-open equilibrium toward the open state. First, at higher lipid concentration, the number and occupancy of ordered lipids increase significantly. Two layers of nearly complete bilayer-like structure fill the grooves between the voltage-sensor-like domains of RyR1. These are also the regions where the largest conformational changes occur on the cytoplasmic leaflet of the membrane domain around the transmembrane helices S5, S6, and the amphipathic S4S5L helix. Compared to lipids, detergent molecules are less hydrophobic, have different geometry, charge distribution, and shape.[49] Consequently, detergent micelles are much more "wet" than lipid bilayers. The binding of lipids to the transmembrane surface renders its immediate environment more hydrophobic, thereby stabilizing the open state. This suggestion is supported by the second observation that the size of the micelles also increases, providing a more hydrophobic environment to the transmembrane domain.

We observed the stabilization of the open state using a model lipid, POPC, which is a rough approximation of the SR

Please cite this article in press as: Li and Efremov, Lipids modulate the open probability of RyR1 under cryo-EM conditions, Structure (2025), https://doi.org/10.1016/j.str.2025.09.003

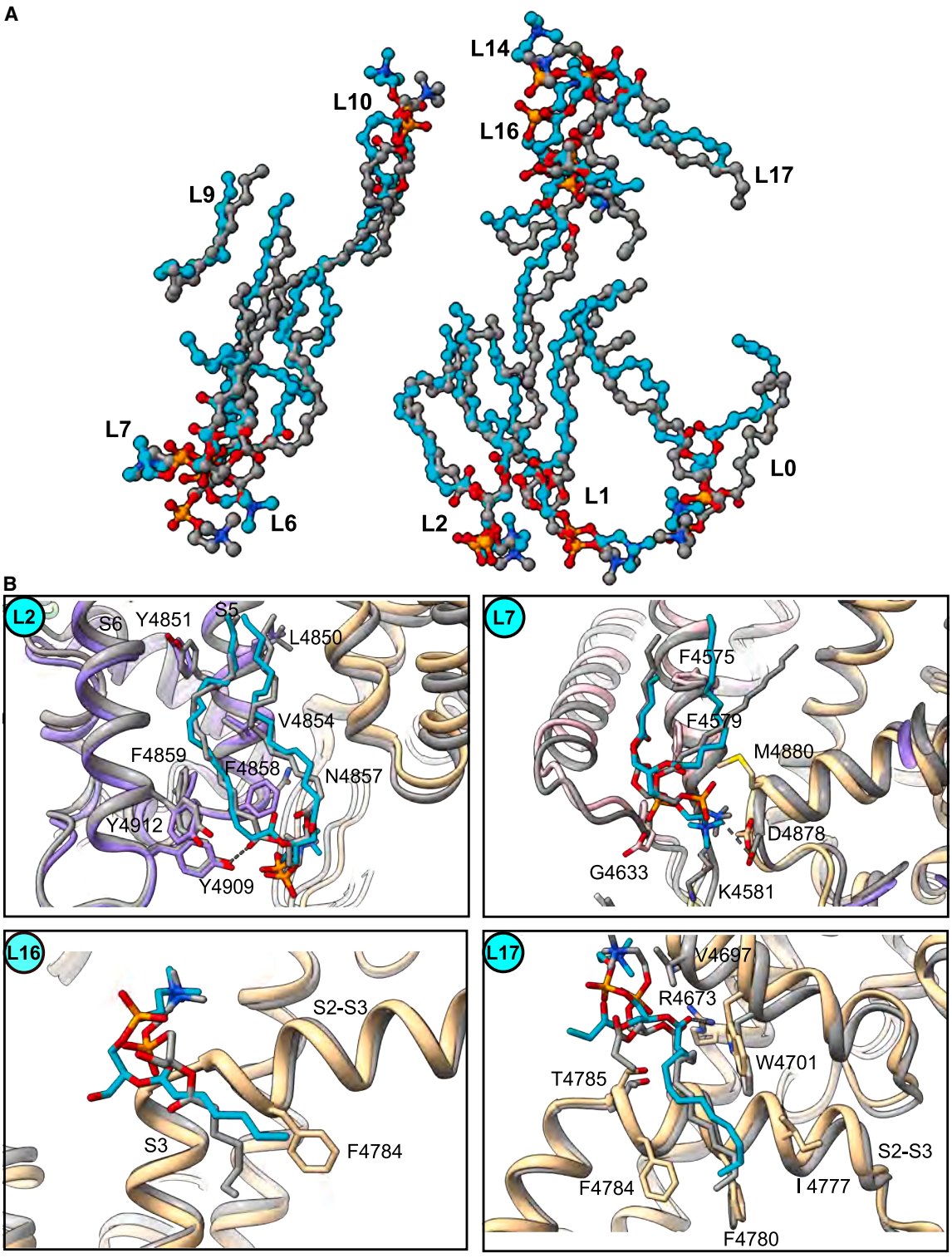

Figure 5. Structural differences in lipid positions between primed and open states

(A) Comparison of lipid models between the DT-0.05-open (gray) and DT-0.05-primed states (colored as in Figure 3).

(B) Detailed view of lipid rearrangements. The structures were aligned on the pore region (residues 4,820–5,037). Only the lipids resolved in the open and the primed state are shown.

Please cite this article in press as: Li and Efremov, Lipids modulate the open probability of RyR1 under cryo-EM conditions, Structure (2025), https://doi.org/10.1016/j.str.2025.09.003

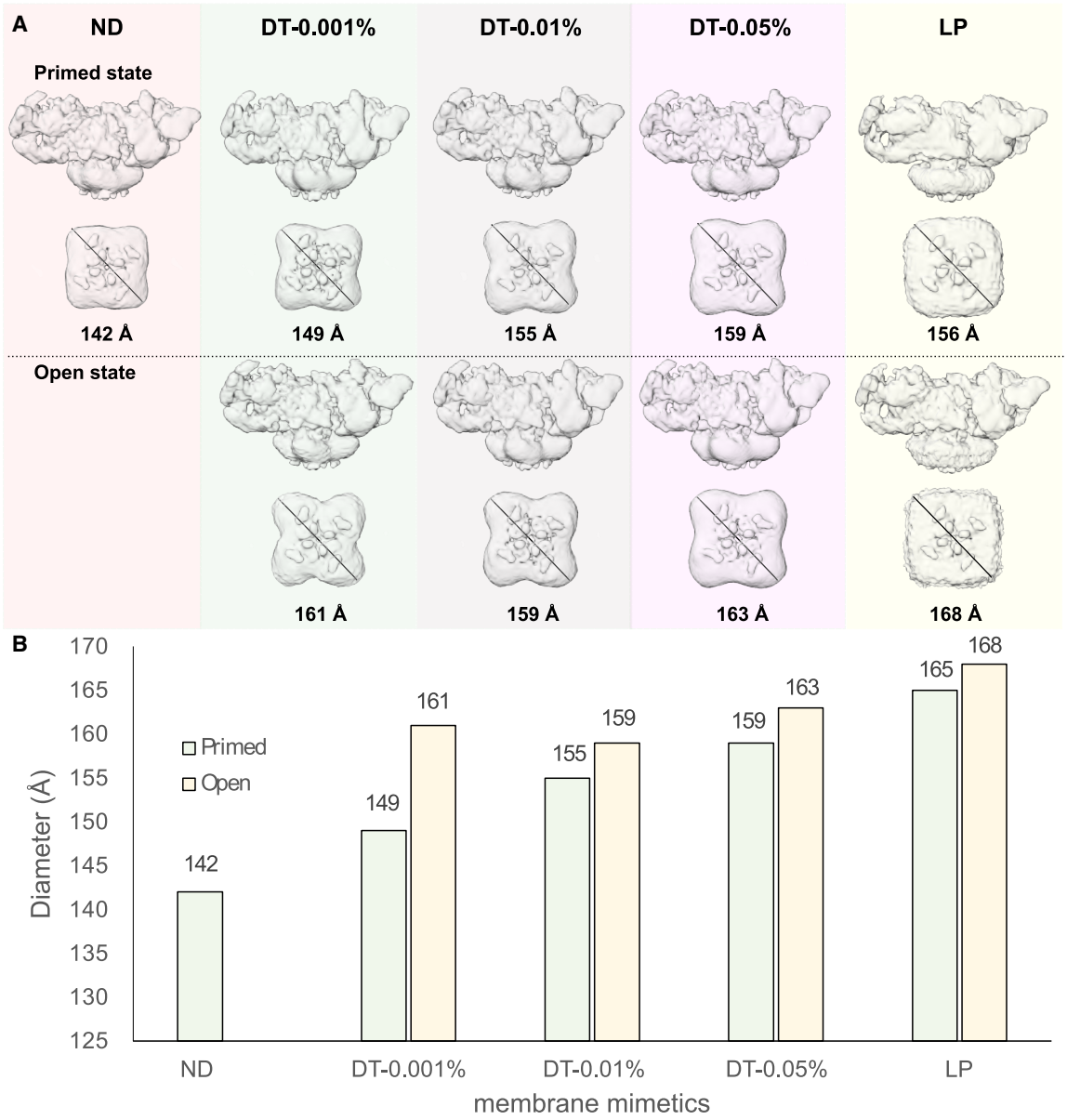

Figure 6. Maps of hydrophobic belts for RyR1 reconstituted in various lipid bilayer mimetics

(A) Density maps of RyR1 in various lipid bilayer mimetics. From left to right: ND, DT-0.001, DT-0.01, DT-0.05, and LP. The first two rows display side and bottom views of the primed state maps, and the third and fourth rows present side and bottom views of the open state maps.

(B) The diameter of the bilayer-mimicking belt for the maps shown in (A).

membrane that also contains phosphatidylethanolamine (PE), phosphatidylserine (PS), sphingolipids, and phosphatidylinositol as principal lipid species.[50] Although we expect that the observed effect is rather generic, since membrane protein function is generally independent of lipid composition,[51] except for signaling,[21] future experimental studies of the channel opening in various lipids will be needed to understand the contribution of different lipid types to the observed effect.

When RyR1 was reconstituted into lipid nanodiscs[37] or liposomes,[34] the lipids were less well resolved than in the DT-0.05-open map. And the fraction of the open conformation was lower. In the liposomes, the open fraction was in the range 37%–62%.[34,37] As has been previously discussed in a study by Li et al.[37] and the aforementioned text, the exact fraction of open channels may be influenced by the lipid composition of liposomes, residual amounts of CHAPS, FKBP12, and the bound nanobody. Lipid bilayer curvature, particularly pronounced in small-diameter liposomes used for cryo-EM, might be another factor modulating the open-primed channel equilibrium[52] and explaining the reduced fraction of open RyR1 channels in the liposomes relative to the CHAPS:POPC mixture.

Intriguingly, reconstituted into lipid nanodiscs, RyR1 was expected to be in a lipid bilayer-like environment[53,54]; however, the channel remained fully closed despite various attempts to open it. RyR1 was reconstituted into lipid nanodiscs using membrane scaffold protein MSP1E3D1 and POPC. To reduce aggregation of the reconstituted RyR1, we added 0.06% fluorinated octyl maltoside (fOM).[37] To open the channel, we attempted to remove fOM and change the nanodiscs' lipid composition from POPC to either SoyPC or a 1:1 mix of POPC and 1,2-dilauroyl-sn-glycero-3-phosphocholine (DLPC),[55] but the channel remained closed. Ryanodine stabilizes RyR1-ND in the fully open state,[18] suggesting that RyR1-ND can be opened but requires a stronger agonist. Consistently, RyR1-ND had the smallest hydrophobic belt among the studied lipid mimetics (Figure 6). The estimated size of the nanodisc of 142 Å is consistent with the expected diameter of MSP1E3D1-based nanodisc (120–160 Å[56]), and its shape suggests that the grooves between voltage-sensor-like domains are filled with lipids. We can hypothesize that in the nanodisc, the lipid belt constrained by MSP1E3D1 is too thin to mimic the bulk of a lipid bilayer. Additionally, direct MSP-RyR1 interactions may further stabilize the closed pore conformation. Similar behavior has been observed for ABC transporters, where nanodiscs restricted conformational states to those more compact relative to detergent micelles.[20] A larger diameter MSP2N2 (~17 nm[57]) was found to be effective in stabilizing the wide conformation of the ATP-Binding Cassette (ABC) transporter[20] and might permit the opening of the RyR1 channel.

The observed dependence of open RyR1 fraction on lipid concentration means that quantitative cryo-EM studies of RyR1 modulation should ensure consistency of lipid concentration in the preparations of cryo-EM samples with and without modulators. Commonly used protein concentrating using porous-membrane-based spin concentrators often concentrates both detergent and lipids,[58] and might lead to variability in the final detergent and lipid concentrations. Alternative RyR1 preparation protocols that do not involve spin concentrators[37] may be considered.

In summary, this report demonstrates that the open probability of RyR1 is highly sensitive to the lipid bilayer mimetics and must be thoroughly controlled during sample preparation for cryo-EM studies that investigate fine regulation of RyR1 gating by modulators. Adjusting lipid concentration in CHAPS-solubilized RyR1 offers a method to fine-tune RyR1 open fraction, matching the purpose of specific structural studies.

RESOURCE AVAILABILITY

Lead contact

Requests for further information and resources should be directed to and will be fulfilled by the lead contact Rouslan G. Efremov (rouslan.efremov@vub.be).

Materials availability

This study did not generate new unique reagents.

Data and code availability

- The cryo-EM maps reported in this paper, including DT-0.01-primed, DT-0.01-open, DT-0.05-primed, and DT-0.05-open have been deposited in the Electron Microscopy Data Bank under accession codes EMDB: EMD-53924, EMD-52091, EMD-53834, and EMD-52085, respectively. The corresponding atomic coordinates have been deposited in the Protein DataBank (PDB) under accession codes PDB: 9RCW, 9HEQ, 9R8O, and 9HEO, respectively. All EMDB- and PDB-deposited data are publicly available as of the date of publication. Other maps and structures referenced in this paper include ND, DT-0.001-primed, DT-0.001-open, and LP-primed with EMBD codes EMDB: EMD-19468, EMD-19472, EMD-19467, and EMD-19465. The corresponding PDB codes are 8RRX, 8RSO, 8RRW, and 8RRU, respectively.
- Any additional information required to reanalyze the data reported in this paper is available from the lead contact upon request.
- This paper does not report original code.

ACKNOWLEDGMENTS

We thank Annelore Stroobants for technical support and Dr. Marcus Fislage for assistance with cryo-EM data collections. This work was funded by grants from FWO (grant nos. G.0266.15N, G0H5916N, and G054617N to R.G.E.) and the European Research Council (grant no. 726436 to R.G.E).

AUTHOR CONTRIBUTIONS

Conceptualization, C.L. and R.G.E.; data curation, C.L.; formal analysis, C.L and R.G.E.; funding acquisition, R.G.E.; investigation, C.L.; methodology, C.L.; project administration, R.G.E.; supervision, R.G.E.; validation, C.L. and R.G.E.; visualization, C.L. and R.G.E.; writing – original draft, C.L.; writing – review & editing, C.L and R.G.E.

DECLARATION OF INTERESTS

The authors declare no competing interests.

STAR★METHODS

Detailed methods are provided in the online version of this paper and include the following:

- KEY RESOURCES TABLE
- EXPERIMENTAL MODEL AND STUDY PARTICIPANT DETAILS
- METHOD DETAILS
  - Rabbit skeletal SR membranes isolation
  - Preparation of Nb-containing periplasmic extract
  - Nanobody-based affinity ryanodine receptor 1 purification
  - Preparation of cryo-EM grids
  - Data collection
  - Cryo-EM data processing
  - Model building and analysis
- QUANTIFICATION AND STATISTICAL ANALYSIS

SUPPLEMENTAL INFORMATION

Supplemental information can be found online at https://doi.org/10.1016/j.str.2025.09.003.

Received: December 3, 2024
Revised: May 31, 2025
Accepted: September 3, 2025

REFERENCES

1. Wu, J., Yan, Z., Li, Z., Qian, X., Lu, S., Dong, M., Zhou, Q., and Yan, N. (2016). Structure of the voltage-gated calcium channel Ca(v)1.1 at 3.6 Å resolution. Nature *537*, 191–196. https://doi.org/10.1038/nature19321.
2. Fan, X., Huang, J., Jin, X., and Yan, N. (2023). Cryo-EM structure of human voltage-gated sodium channel Nav1.6. Proc. Natl. Acad. Sci. USA *120*, e2220578120. https://doi.org/10.1073/pnas.2220578120.
3. Hite, R.K., Yuan, P., Li, Z., Hsuing, Y., Walz, T., and MacKinnon, R. (2015). Cryo-electron microscopy structure of the Slo2.2 Na(+)-activated K(+) channel. Nature *527*, 198–203. https://doi.org/10.1038/nature14958.

4. Vénien-Bryan, C., and Fernandes, C.A.H. (2023). Overview of Membrane Protein Sample Preparation for Single-Particle Cryo-Electron Microscopy Analysis. Int. J. Mol. Sci. *24*, 14785. https://doi.org/10.3390/ijms241914785.

5. Fu, Z., and MacKinnon, R. (2024). Structure of the flotillin complex in a native membrane environment. Proc. Natl. Acad. Sci. USA *121*, e2409334121. https://doi.org/10.1073/pnas.2409334121.

6. Huynh, K.W., Cohen, M.R., and Moiseenkova-Bell, V.Y. (2014). Application of amphipols for structure-functional analysis of TRP channels. J. Membr. Biol. *247*, 843–851. https://doi.org/10.1007/s00232-014-9684-6.

7. Gao, Y., Cao, E., Julius, D., and Cheng, Y. (2016). TRPV1 structures in nanodiscs reveal mechanisms of ligand and lipid action. Nature *534*, 347–351. https://doi.org/10.1038/nature17964.

8. Yao, X., Fan, X., and Yan, N. (2020). Cryo-EM analysis of a membrane protein embedded in the liposome. Proc. Natl. Acad. Sci. USA *117*, 18497–18503. https://doi.org/10.1073/pnas.2009385117.

9. Xu, J., Liao, C., Yin, C.-C., Li, G., Zhu, Y., and Sun, F. (2024). In situ structural insights into the excitation-contraction coupling mechanism of skeletal muscle. Sci. Adv. *10*, eadl1126. https://doi.org/10.1126/sciadv.adl1126.

10. Efremov, R.G., Leitner, A., Aebersold, R., and Raunser, S. (2015). Architecture and conformational switch mechanism of the ryanodine receptor. Nature *517*, 39–43. https://doi.org/10.1038/nature13916.

11. Efremov, R.G., Gatsogiannis, C., and Raunser, S. (2017). Lipid Nanodiscs as a Tool for High-Resolution Structure Determination of Membrane Proteins by Single-Particle Cryo-EM BT - A Structure-Function Toolbox for Membrane Transporter and Channels. In A Structure-Function Toolbox for Membrane Transporter and Channels (Elsevier), pp. 1–30. https://doi.org/10.1016/bs.mie.2017.05.007.

12. Fan, G., Baker, M.R., Terry, L.E., Arige, V., Chen, M., Seryshev, A.B., Baker, M.L., Ludtke, S.J., Yule, D.I., and Serysheva, I.I. (2022). Conformational motions and ligand-binding underlying gating and regulation in IP3R channel. Nat. Commun. *13*, 6942. https://doi.org/10.1038/s41467-022-34574-1.

13. des Georges, A., Clarke, O.B., Zalk, R., Yuan, Q., Condon, K.J., Grassucci, R.A., Hendrickson, W.A., Marks, A.R., and Frank, J. (2016). Structural Basis for Gating and Activation of RyR1. Cell *167*, 145–157.e17. https://doi.org/10.1016/j.cell.2016.08.075.

14. Blesneac, I., Chemin, J., Bidaud, I., Huc-Brandt, S., Vandermoere, F., and Lory, P. (2015). Phosphorylation of the Cav3.2 T-type calcium channel directly regulates its gating properties. Proc. Natl. Acad. Sci. USA *112*, 13705–13710. https://doi.org/10.1073/pnas.1511740112.

15. Harraz, O.F., and Welsh, D.G. (2013). Protein kinase A regulation of T-type Ca2+ channels in rat cerebral arterial smooth muscle. J. Cell Sci. *126*, 2944–2954. https://doi.org/10.1242/jcs.128363.

16. Foskett, J.K., and Daniel Mak, D.-O. (2010). Regulation of IP(3)R Channel Gating by Ca(2+) and Ca(2+) Binding Proteins. Curr. Top. Membr. *66*, 235–272. https://doi.org/10.1016/S1063-5823(10)66011-5.

17. Biou, V. (2023). Lipid-membrane protein interaction visualised by cryo-EM: A review. Biochim. Biophys. Acta. Biomembr. *1865*, 184068. https://doi.org/10.1016/j.bbamem.2022.184068.

18. Willegems, K., and Efremov, R.G. (2018). Influence of Lipid Mimetics on Gating of Ryanodine Receptor. Structure *26*, 1303–1313.e4. https://doi.org/10.1016/j.str.2018.06.010.

19. Jiang, Q.-X., and Gonen, T. (2012). The influence of lipids on voltage-gated ion channels. Curr. Opin. Struct. Biol. *22*, 529–536. https://doi.org/10.1016/j.sbi.2012.03.009.

20. Hoffmann, L., Baier, A., Jorde, L., Kamel, M., Schäfer, J.-H., Schnelle, K., Scholz, A., Shvarev, D., Wong, J.E.M.M., Parey, K., et al. (2025). The ABC transporter MsbA in a dozen environments. Structure *33*, 916–923.e4. https://doi.org/10.1016/j.str.2025.02.002.

21. Saponaro, A., and Lolicato, M. (2022). Editorial: The key role of lipids in the regulation of ion channels. Front. Physiol. *13*, 1000082. https://doi.org/10.3389/fphys.2022.1000082.

22. Capes, E.M., Loaiza, R., and Valdivia, H.H. (2011). Ryanodine receptors. Skelet. Muscle *1*, 18. https://doi.org/10.1186/2044-5040-1-18.

23. Woll, K.A., and Van Petegem, F. (2022). Calcium-release channels: structure and function of IP3 receptors and ryanodine receptors. Physiol. Rev. *102*, 209–268. https://doi.org/10.1152/physrev.00033.2020.

24. Van Petegem, F., and Lau, K. (2012). Ryanodine Receptor (RyR). In Encyclopedia of Signaling Molecules (Springer), pp. 1704–1709. https://doi.org/10.1007/978-1-4419-0461-4_99.

25. Lanner, J.T., Georgiou, D.K., Joshi, A.D., and Hamilton, S.L. (2010). Ryanodine receptors: structure, expression, molecular details, and function in calcium release. Cold Spring Harb. Perspect. Biol. *2*, a003996. https://doi.org/10.1101/cshperspect.a003996.

26. Van Petegem, F. (2012). Ryanodine Receptors: Structure and Function. J. Biol. Chem. *287*, 31624–31632. https://doi.org/10.1074/jbc.R112.349068.

27. Shishmarev, D. (2020). Excitation-contraction coupling in skeletal muscle: recent progress and unanswered questions. Biophys. Rev. *12*, 143–153. https://doi.org/10.1007/s12551-020-00610-x.

28. Bolaños, P., and Calderón, J.C. (2022). Excitation-contraction coupling in mammalian skeletal muscle: Blending old and last-decade research. Front. Physiol. *13*, 989796. https://doi.org/10.3389/fphys.2022.989796.

29. Quane, K.A., Healy, J.M., Keating, K.E., Manning, B.M., Couch, F.J., Palmucci, L.M., Doriguzzi, C., Fagerlund, T.H., Berg, K., and Ording, H. (1993). Mutations in the ryanodine receptor gene in central core disease and malignant hyperthermia. Nat. Genet. *5*, 51–55. https://doi.org/10.1038/ng0993-51.

30. Davis, M.R., Haan, E., Jungbluth, H., Sewry, C., North, K., Muntoni, F., Kuntzer, T., Lamont, P., Bankier, A., Tomlinson, P., et al. (2003). Principal mutation hotspot for central core disease and related myopathies in the C-terminal transmembrane region of the RYR1 gene. Neuromuscul. Disord. *13*, 151–157. https://doi.org/10.1016/s0960-8966(02)00218-3.

31. Laver, D.R. (2018). Regulation of the RyR channel gating by Ca2+ and Mg2. Biophys. Rev. *10*, 1087–1095. https://doi.org/10.1007/s12551-018-0433-4.

32. Peng, W., Shen, H., Wu, J., Guo, W., Pan, X., Wang, R., Chen, S.R.W., and Yan, N. (2016). Structural basis for the gating mechanism of the type 2 ryanodine receptor RyR2. Science *354*, aah5324. https://doi.org/10.1126/science.aah5324.

33. Cholak, S., Saville, J.W., Zhu, X., Berezuk, A.M., Tuttle, K.S., Haji-Ghassemi, O., Alvarado, F.J., Van Petegem, F., and Subramaniam, S. (2023). Allosteric modulation of ryanodine receptor RyR1 by nucleotide derivatives. Structure *31*, 790–800.e4. https://doi.org/10.1016/j.str.2023.04.009.

34. Melville, Z., Kim, K., Clarke, O.B., and Marks, A.R. (2022). High-resolution structure of the membrane-embedded skeletal muscle ryanodine receptor. Structure *30*, 172–180.e3. https://doi.org/10.1016/j.str.2021.08.001.

35. Melville, Z., Dridi, H., Yuan, Q., Reiken, S., Wronska, A., Liu, Y., Clarke, O.B., and Marks, A.R. (2022). A drug and ATP binding site in type 1 ryanodine receptor. Structure *30*, 1025–1034.e4. https://doi.org/10.1016/j.str.2022.04.010.

36. Kim, K., Li, H., Yuan, Q., Melville, Z., Zalk, R., des Georges, A., Frank, J., Hendrickson, W.A., Marks, A.R., and Clarke, O.B. (2024). Structural identification of the RY12 domain of RyR1 as an ADP sensor and the target of the malignant hyperthermia therapeutic dantrolene. Preprint at bioRxiv. https://doi.org/10.1101/2024.10.21.619409.

37. Li, C., Willegems, K., Uchański, T., Pardon, E., Steyaert, J., and Efremov, R.G. (2024). Rapid small-scale nanobody-assisted purification of ryanodine receptors for cryo-EM. J. Biol. Chem. *300*, 107734. https://doi.org/10.1016/j.jbc.2024.107734.

38. Smart, O.S., Neduvelil, J.G., Wang, X., Wallace, B.A., and Sansom, M.S. (1996). HOLE: A program for the analysis of the pore dimensions of ion channel structural models. J. Mol. Graph. *14*, 354–376. https://doi.org/10.1016/S0263-7855(97)00009-X.

39. Chelu, M.G., Danila, C.I., Gilman, C.P., and Hamilton, S.L. (2004). Regulation of ryanodine receptors by FK506 binding proteins. Trends Cardiovasc. Med. *14*, 227–234. https://doi.org/10.1016/j.tcm.2004.06.003.

40. Forsberg, B.O., Shah, P.N.M., and Burt, A. (2023). A robust normalized local filter to estimate compositional heterogeneity directly from cryo-EM maps. Nat. Commun. *14*, 5802. https://doi.org/10.1038/s41467-023-41478-1.

41. Dalal, V., Arcario, M.J., Petroff, J.T., Tan, B.K., Dietzen, N.M., Rau, M.J., Fitzpatrick, J.A.J., Brannigan, G., and Cheng, W.W.L. (2024). Lipid nanodisc scaffold and size alter the structure of a pentameric ligand-gated ion channel. Nat. Commun. *15*, 25. https://doi.org/10.1038/s41467-023-44366-w.

42. Salentin, S., Schreiber, S., Haupt, V.J., Adasme, M.F., and Schroeder, M. (2015). PLIP: fully automated protein-ligand interaction profiler. Nucleic Acids Res. *43*, W443–W447. https://doi.org/10.1093/nar/gkv315.

43. Nayak, A.R., and Samsó, M. (2022). Ca 2+ inactivation of the mammalian ryanodine receptor type 1 in a lipidic environment revealed by cryo-EM. Elife *11*, e75568. https://doi.org/10.7554/eLife.75568.

44. Monnier, N., Romero, N.B., Lerale, J., Landrieu, P., Nivoche, Y., Fardeau, M., and Lunardi, J. (2001). Familial and sporadic forms of central core disease are associated with mutations in the C-terminal domain of the skeletal muscle ryanodine receptor. Hum. Mol. Genet. *10*, 2581–2592. https://doi.org/10.1093/hmg/10.22.2581.

45. Kossugue, P.M., Paim, J.F., Navarro, M.M., Silva, H.C., Pavanello, R.C.M., Gurgel-Giannetti, J., Zatz, M., and Vainzof, M. (2007). Central core disease due to recessive mutations in RYR1 gene: is it more common than described? Muscle Nerve *35*, 670–674. https://doi.org/10.1002/mus.20715.

46. Chen, S.R., Leong, P., Imredy, J.P., Bartlett, C., Zhang, L., and MacLennan, D.H. (1997). Single-channel properties of the recombinant skeletal muscle Ca2+ release channel (ryanodine receptor). Biophys. J. *73*, 1904–1912. https://doi.org/10.1016/S0006-3495(97)78221-3.

47. Santonastasi, M., and Wehrens, X.H.T. (2007). Ryanodine receptors as pharmacological targets for heart disease. Acta Pharmacol. Sin. *28*, 937–944. https://doi.org/10.1111/j.1745-7254.2007.00582.x.

48. Bai, X.-C., Yan, Z., Wu, J., Li, Z., and Yan, N. (2016). The Central domain of RyR1 is the transducer for long-range allosteric gating of channel opening. Cell Res. *26*, 995–1006. https://doi.org/10.1038/cr.2016.89.

49. Zhou, H.-X., and Cross, T.A. (2013). Influences of Membrane Mimetic Environments on Membrane Protein Structures. Annu. Rev. Biophys. *42*, 361–392. https://doi.org/10.1146/annurev-biophys-083012-130326.

50. Borchman, D., Tang, D., and Yappert, M.C. (1999). Lipid composition, membrane structure relationships in lens and muscle sarcoplasmic reticulum membranes. Biospectroscopy *5*, 151–167. https://doi.org/10.1002/(SICI)1520-6343(1999)5:3<151::AID-BSPY5>3.0.CO;2-D.

51. Sanders, C.R., and Mittendorf, K.F. (2011). Tolerance to changes in membrane lipid composition as a selected trait of membrane proteins. Biochemistry *50*, 7858–7867. https://doi.org/10.1021/bi2011527.

52. Damm, A., Paik, S.-J., Sadhu, R.K., Di-Cicco, A., Manzi, J., Castellana, M., Margeat, E., Dahan, M., Sens, P., Lévy, D., and Bassereau, P. (2024). Conformational changes of the ABC Transporter BmrA Depend on Membrane Curvature. Preprint at bioRxiv. https://doi.org/10.1101/2024.01.24.577054.

53. Efremov, R.G., Gatsogiannis, C., and Raunser, S. (2017). Lipid Nanodiscs as a Tool for High-Resolution Structure Determination of Membrane Proteins by Single-Particle Cryo-EM. Methods Enzymol. *594*, 1–30. https://doi.org/10.1016/bs.mie.2017.05.007.

54. Ritchie, T.K., Grinkova, Y.V., Bayburt, T.H., Denisov, I.G., Zolnerciks, J.K., Atkins, W.M., and Sligar, S.G. (2009). Chapter 11 - Reconstitution of membrane proteins in phospholipid bilayer nanodiscs. Methods Enzymol. *464*, 211–231. https://doi.org/10.1016/S0076-6879(09)64011-8.

55. Odorčić, I., Hamed, M.B., Lismont, S., Chávez-Gutiérrez, L., and Efremov, R.G. (2024). Apo and Aβ46-bound γ-secretase structures provide insights into amyloid-β processing by the APH-1B isoform. Nat. Commun. *15*, 4479. https://doi.org/10.1038/s41467-024-48776-2.

56. Denisov, I.G., and Sligar, S.G. (2016). Nanodiscs for structural and functional studies of membrane proteins. Nat. Struct. Mol. Biol. *23*, 481–486. https://doi.org/10.1038/nsmb.3195.

57. Grinkova, Y.V., Denisov, I.G., and Sligar, S.G. (2010). Engineering extended membrane scaffold proteins for self-assembly of soluble nanoscale lipid bilayers. Protein Eng. Des. Sel. *23*, 843–848. https://doi.org/10.1093/protein/gzq060.

58. Gobet, A., Zampieri, V., Magnard, S., Pebay-Peyroula, E., Falson, P., and Chaptal, V. (2023). The non-Newtonian behavior of detergents during concentration is increased by macromolecules, in trans, and results in their over-concentration. Biochimie *205*, 53–60. https://doi.org/10.1016/j.biochi.2022.09.004.

59. Punjani, A., Rubinstein, J.L., Fleet, D.J., and Brubaker, M.A. (2017). cryoSPARC: algorithms for rapid unsupervised cryo-EM structure determination. Nat. Methods *14*, 290–296. https://doi.org/10.1038/nmeth.4169.

60. Kimanius, D., Dong, L., Sharov, G., Nakane, T., and Scheres, S.H.W. (2021). New tools for automated cryo-EM single-particle analysis in RELION-4.0. Biochem. J. *478*, 4169–4185. https://doi.org/10.1042/BCJ20210708.

61. Afonine, P.V., Headd, J.J., and Terwilliger, T.C. (2013). New tool: phenix.real_space_refine. Comput. Crystallogr. Newsl. *4*, 43–44.

62. Emsley, P., and Cowtan, K. (2004). Coot: model-building tools for molecular graphics. Acta Crystallogr. D Biol. Crystallogr. *60*, 2126–2132. https://doi.org/10.1107/S0907444904019158.

63. Pettersen, E.F., Goddard, T.D., Huang, C.C., Meng, E.C., Couch, G.S., Croll, T.I., Morris, J.H., and Ferrin, T.E. (2021). UCSF ChimeraX: Structure visualization for researchers, educators, and developers. Protein Sci. *30*, 70–82. https://doi.org/10.1002/pro.3943.

64. Fislage, M., Shkumatov, A.V., Stroobants, A., and Efremov, R.G. (2020). Assessing the JEOL CRYO ARM 300 for high-throughput automated single-particle cryo-EM in a multiuser environment. IUCrJ *7*, 707–718. https://doi.org/10.1107/S2052252520006065.

65. Mastronarde, D.N. (2005). Automated electron microscope tomography using robust prediction of specimen movements. J. Struct. Biol. *152*, 36–51. https://doi.org/10.1016/j.jsb.2005.07.007.

66. Efremov, R.G., and Stroobants, A. (2021). Coma-corrected rapid single-particle cryo-EM data collection on the CRYO ARM 300. Acta Crystallogr. D Struct. Biol. *77*, 555–564. https://doi.org/10.1107/S2059798321002151.

67. Zheng, S.Q., Palovcak, E., Armache, J.-P., Verba, K.A., Cheng, Y., and Agard, D.A. (2017). MotionCor2: anisotropic correction of beam-induced motion for improved cryo-electron microscopy. Nat. Methods *14*, 331–332. https://doi.org/10.1038/nmeth.4193.

68. Rohou, A., and Grigorieff, N. (2015). CTFFIND4: Fast and accurate defocus estimation from electron micrographs. J. Struct. Biol. *192*, 216–221. https://doi.org/10.1016/j.jsb.2015.08.008.

69. Tung, C.-C., Lobo, P.A., Kimlicka, L., and Van Petegem, F. (2010). The amino-terminal disease hotspot of ryanodine receptors forms a cytoplasmic vestibule. Nature *468*, 585–588. https://doi.org/10.1038/nature09471.

70. Williams, C.J., Headd, J.J., Moriarty, N.W., Prisant, M.G., Videau, L.L., Deis, L.N., Verma, V., Keedy, D.A., Hintze, B.J., Chen, V.B., et al. (2018). MolProbity: More and better reference data for improved all-atom structure validation. Protein Sci. *27*, 293–315. https://doi.org/10.1002/pro.3330.

Please cite this article in press as: Li and Efremov, Lipids modulate the open probability of RyR1 under cryo-EM conditions, Structure (2025), https://doi.org/10.1016/j.str.2025.09.003

STAR★METHODS

KEY RESOURCES TABLE

REAGENT or RESOURCE	SOURCE	IDENTIFIER
Chemicals, peptides, and recombinant proteins		
CHAPS	Anatrace	Cat #c316s, cas # 75621-03-3
POPC	Sigma-Aldrich	Cat # 850457c
Critical commercial assays		
Pierce™ 660nm protein assay	Thermo Fisher Scientific	Cat # 22660
Hispur NI-NTA magnetic beads	Thermo Fisher Scientific	Cat # 88832
Deposited data		
ND	Li et al.[37]	PDB: 8RRX, EMDB: 19468
DT-0.001-primed	Li et al.[37]	PDB: 8RSO, EMDB: 19472
DT-0.001-open	Li et al.[37]	PDB: 8RRW, EMDB: 19467
DT-0.01-primed	This study	PDB:9RCW, EMDB:53924
DT1-0.01-open	This study	PDB:9HEQ, EMDB:52091
DT-0.05-primed	This study	PDB:9R8O, EMDB:53834
DT-0.05-open	This study	PDB:9HEO, EMDB:52085
LP-primed	Li et al., 2024	PDB:8RRU, EMDB: 19465
Experimental models: Organisms/strains		
New Zealand albino rabbit (8–12 weeks old)	Pel-Freez Biologicals	Cat # 41225
Software and algorithms		
cryoSPARC	Punjaniet al.[59]	Https://cryosparc.com/; rrid: scr_016501
Relion	Kimanius et al.[60]	https://www3.mrc-lmb.cam.ac.uk/relion/index.php?title=main_page; rrid: scr_016274
PHENIX	Afonine et al.[61]	https://www.phenix-online.org/; rrid: scr_014224
COOT	Emsley at al.[62]	https://www.ccpem.ac.uk/; rrid: scr_014222
HOLE	Smart et al.[38]	http://www.holeprogram.org/
ChimeraX	Pettersen et al.[63]	https://www.cgl.ucsf.edu/chimerax/; rrid: scr_015872
Other		
Ultraufoil holey gold grids	Quantifoil	R2/1, Cu 300
Graphene oxide	Sigma	Cat # 900704

EXPERIMENTAL MODEL AND STUDY PARTICIPANT DETAILS

Rabbit tissue used for the purification of RyR1 was New Zealand albino rabbit, 8–12 weeks old, gender unspecified, purchased from Pel-Freez Biologicals.

METHOD DETAILS

Rabbit skeletal SR membranes isolation

The method used for SR membrane isolation here is adapted from a previously described protocol.[10] All steps were conducted on ice or at 4°C. Around 120 g of muscle tissue from a male New Zealand White rabbit of 8 weeks old was diced into ~1 cm^3 cubes and homogenized in 1.6 L ice-cold buffer (20 mM Tris-maleate pH 7.0, 100 mM NaCl, 0.3 M sucrose, 1 mM EGTA, 2 mM DTT, and a cocktail of inhibitors: 4 mM leupeptine, 1 mM benzamidine, 0.1 mM aprotinin, 1 mM pepstatin, 2 mM calpain I inhibitor and 1 mM phenylmethylsulphonyl fluoride (PMSF)) using a Waring blender. The homogenization was performed in bursts with a duration of 30 s each until the homogenized suspension appeared pink and smooth. Then the suspension was centrifuged for 30 min at 7,000 rpm, in a Beckman *JA-10* rotor. The supernatant was filtered through two layers of cheesecloth, and 0.5 M KCl was added and stirred for at least 10 min. The extract was centrifuged at 40,000 rpm for 30 min in a Beckman 45Ti rotor. The pellet was resuspended in buffer containing 20 mM MOPS, pH 7.4, 1 mM EGTA, 2 mM DTT, 0.6 M KCl, 0.3 M sucrose, and cocktail of inhibitors to a final volume of

Please cite this article in press as: Li and Efremov, Lipids modulate the open probability of RyR1 under cryo-EM conditions, Structure (2025), https://doi.org/10.1016/j.str.2025.09.003

80–100 mL using a glass homogenizer and centrifuged at 40,000 rpm for 30 min in Beckman 45Ti rotor. The pellets were homogenized in the resuspension buffer to a concentration of around 10 mg/mL, frozen in liquid nitrogen, and stored at −80°C. Protein concentration was determined by Pierce 660 nm protein assay (Thermo Fisher Scientific).

Preparation of Nb-containing periplasmic extract

The nanobody was cloned into the phage-display vector pMESy4, facilitating the expression of Nbs with a 6xHis-tag. Overexpression of Nbs occurred overnight following induction with 1 mM Isopropyl β-D-1-thiogalactopyranoside (IPTG) in *Escherichia coli* WK6 strain, initiated once the cell density reached OD600 of 0.8. Cells were harvested by centrifugation at 5,000 rpm for 15 min using a Beckman JA-10 rotor. The cell pellet was lysed by adding 4 mL of lysis buffer (50 mM Tris pH 7.5, 150 mM NaCl, 1 mM EDTA, 0.1 mg/mL lysozyme, 20% sucrose, 50 μg/mL DNase, and 1 mM PMSF) per 1 g of pellet, followed by a 30 min incubation at 4°C. Periplasmic extract was obtained by centrifugation at 10,000 rpm for 15 min using a Beckman JA-20 rotor. $MgCl_2$ (5 mM) was added to the extract, followed by filtration through a 0.45 μm Millipore filter and supplementation with 20% sucrose before storage at −80°C in aliquots.

Nanobody-based affinity ryanodine receptor 1 purification

Every step of the purification was performed at 4°C or on ice. 0.5 mL of SR membranes (10 mg/mL) was solubilized by 375 μL solubilization buffer (20 mM MOPS pH7.4, 1 M NaCl, 10% sucrose, 2 mM TECP, 4% CHAPS 0.8% POPC, and a cocktail of protease inhibitors) for at least 30 min following 30 min ultracentrifugation at 40,000 rpm in Beckman 50.4 Ti rotor. Then, the supernatant was incubated with nanobody-loaded magnetic beads for 30 min and washed with SBL buffer (similar to solubilization buffer except for 0.7 M NaCl, 0.8% CHAPS, 0.2% POPC, and 200 μM EGTA). Nanobody-loaded magnetic beads (HisPur Ni-NTA Magnetic Beads, Thermo Fisher Scientific) were prepared by incubating 135 μL washed magnetic beads with 135 μL Nb9657-His periplasmic extract for 15 min. Magnetic beads were equilibrated and washed with SBL buffer by adding 270 μL SBL buffer. The first elution was done by incubating 65 μL elution buffer 1 (SBL buffer with 500 mM Imidazole) with magnetic beads for 5 min. At the second purification step, 65 μL of eluate was diluted with 600 μL SBL buffer, and the mix was incubated for 30 min with another 135 μL of Nb9657 loaded magnetic beads. After incubation, the beads were washed three times with SBL buffer.

Second elution was performed by incubating the beads with 60 μL of elution buffer 2 (SBL buffer with 2 mM ATP, 5 mM caffeine, and 50 μM free Ca^{2+} and 500 mM imidazole), followed by separating the beads from the eluate using a magnetic stand. The elution 2 was then applied to the homemade spin column equilibrated in desalting buffer 1 (elution buffer 2 without imidazole) and centrifuged for 1 min at 1000 x g to remove imidazole. After the first desalting step, 50 μL of eluate was incubated with 60 μg of Mb9657 for at least 1h. The desalting was repeated using desalting buffer 2 (similar to desalting buffer 1, the NaCl concentration was 0.2 M with either 0.2% CHAPS and 0.05% POPC or 0.2% CHAPS and 0.01% POPC).

Preparation of cryo-EM grids

Home-made graphene oxide grids were prepared as described elsewhere.[37] The cryo-EM samples were prepared using a CP3 cryoplunge system (Gatan). A 4 μL aliquot of the protein solution was applied to the carbon side, while 1 μL of desalting buffer without detergent and lipids was added to the copper side of the grid. Blotting from both sides was performed for 1.2 s using Whatman glass microfiber filter paper GF/A at 91% relative humidity. The grids were plunge-frozen in liquid ethane at −175°C and then stored in liquid nitrogen.

Data collection

Cryo-EM images were acquired using a JEOL CryoARM300 microscope, with an in-column Ω energy filter and a cold field emission gun operating at 300 kV.[64] Images were collected on a K3 detector (Gatan). Movies comprising 60 frames at a nominal magnification of 60,000× were automatically captured using SerialEM 3.0.8.[65] The energy filter slit was set to a width of 20 eV. Each frame had an exposure time of 2.796 s, with an average dose per frame of 1 electron per square angstrom (1 $e^-/Å^2$), and defocus values ranging from −1.5 to −2.5 μm. The pixel sizes ranged from 0.73 Å to 0.76 Å. A cross-shaped pattern was used to collect 25 images per single stage position (5 per hole), with three holes along each axis.[66]

Cryo-EM data processing

For all datasets, motion correction was performed using MotionCor2.[67] Contrast Transfer Function parameters were estimated using CTFFIND-4.1.[68] Subsequently, all images were imported into cryoSPARC (version 4.6.2)[59] for further processing. Particle picking was conducted with the template picker using 2D templates created from already processed datasets. Following particle picking, all particles were extracted into boxes of 168 pixels, with a pixel size of 2.92 Å. Multiple rounds of 2D classification were then performed to select particles for subsequent processing (Figures S1 and S2).

For the ND-0.01 dataset, 128,894 particles were selected after 2D classification to generate an initial model with C1 symmetry. A total of 127,957 particles were re-extracted into 336-pixel boxes with a pixel size of 1.46 Å. These particles were refined into a consensus 3D map with C4 symmetry, achieving a resolution of 3.6 Å. The particles were imported into Relion v4.0.1[60] for polishing and 3D classification.

During the 3D classification, particles were divided into six classes using a mask focused on the transmembrane region (Figure S1) to separate the open and primed states. Classes 1, 2, 4, and 5 represented the open conformation, comprising 80,709 particles.

Please cite this article in press as: Li and Efremov, Lipids modulate the open probability of RyR1 under cryo-EM conditions, Structure (2025), https://doi.org/10.1016/j.str.2025.09.003

Class 3, containing 14,320 particles, corresponded to the primed conformation, while particles contributing to class 6, with poor density, were discarded. The open and primed state particles were imported back into cryoSPARC v4.6.2 for refinement using the NU-Refinement procedure. The consensus maps of the open and primed states were reconstructed to resolutions of 3.6 Å and 3.3 Å, respectively.

To improve the density of flexible domains, four local refinements were performed using local masks (Figure S1). Mask 1 covered TaF, TM, and CTD domains, mask 2- JSolA and CSol, mask 3- FKBP and TTD, and mask 4- BSol.

For the open state, local refinement with mask 1 was applied to the 80,709 particles with C4 symmetry. Masks 2, 3, and 4 were used for local refinement with C1 symmetry on 322,836 particles generated through C4 symmetry expansion of the 80,709 particles. The resulting local maps had resolutions of 3.1 Å (mask 1), 3.2 Å (mask 2), 3.1 Å (mask 3), and 3.9 Å (mask 4).

For the primed state, local refinement with mask 1 was performed on 39,983 particles with C4 symmetry. Masks 2, 3, and 4 were used for local refinement with C1 symmetry on 159,932 particles obtained after C4 symmetry expansion of the 39,983 particles. The resulting local maps had resolutions of 3.4 Å (mask 1), 3.3 Å (mask 2), 3.1 Å (mask 3), and 3.8 Å (mask 4).

The resulting maps were combined in Chimera v1.15 to generate a composite map. Pixel size calibration and model building were performed on the composite map.

The DT-0.05 dataset was processed similarly (Figure S2). A total of 335,432 particles were selected after 2D classification and used to generate an ab initio model with C1 symmetry (Figure S2). The particles were re-extracted into 336-pixel boxes at a pixel size of 1.51 Å and refined into a consensus 3D map with C4 symmetry.

All particles were imported into Relion v4.0.1 for polishing and 3D classification. Six classes were defined for classification: classes 1, 4, and 5 represented the open conformation and comprised 279,776 particles. Class 6 corresponded to the primed conformation, comprising 53,158 particles. Classes 2 and 3 were discarded due to poor density. The consensus map of the open state was reconstructed to a resolution of 3.4 Å, with local maps achieving resolutions of 3.3 Å for masks 1, 2, and 3, and 3.6 Å for mask 4. The consensus map of the primed state was reconstructed to a resolution of 3.6 Å with local maps achieving resolutions of 3.3 Å for mask 1, 3.5 Å for mask 2, 3.3 Å for mask 3, and 4.4 Å for mask 4.

FKBP occupancy estimation by 3D classification was performed in cryoSPARC. Particles from the consensus map were C4 symmetry expanded. The 3D classification was performed on the expanded particles using a mask covering the FKBP domain (green in Figure S5). The mask was generated by fitting an FKBP model into the consensus map, generating a map to 8 Å resolution using the Chimera molmap command, followed by application of a threshold of 0.05, map dilation with a radius of 10 pixels, and soft padding of 15 pixels. The 3D classification was performed using a filter resolution of 12 Å. The resulting maps were low-pass filtered to 8 Å and thresholded (threshold level = 2). Particles were counted in classes showing clear FKBP density within the masked region.

To compare the maps with previous work Li et al.,[37] the pixel size of the maps was calibrated against the N-terminal domain of the 5TAL structure[13] (first 500 residues) by fitting the simulated map of the domain calculated to 6 Å resolution into the reconstructed cryo-EM maps and calculating cross-correlation between the maps in ChimeraX v1.6. The pixel size producing the highest correlation was used for map sharpening in cryoSparc. For map depositions, the pixel size was calibrated relative to the crystal structure of N-terminal domain 2XOA.[69]

Model building and analysis

The initial model of open state PDB: 8RRW and 8RRX for the primed state was used. The initial models were rigid body fit to each map in Chimera v 1.15,[63] then manually rebuilt in Coot 0.98[62] followed by real-space refinement in Phenix 1.20.1[61] using default parameters. All models were validated with MolProbity.[70] The figures were prepared using ChimeraX-1.7.1.[63]

The cross-correlation coefficients between maps and lipid molecules were calculated by fitting the DT-0.05 open model of lipids and the transmembrane domain of RyR1 into corresponding maps and real-space refining the model in Coot. Next, the models were refined by the Phenix real-space refinement routine, and cross-correlation coefficients reported by Phenix model-data validation statistics were plotted.

QUANTIFICATION AND STATISTICAL ANALYSIS

Cryo-EM data collection and refinement statistics are summarized in Table 1. Fractions of open RyR1 were calculated from particle counts after 3D classification in RELION (Figure 2; Table S2). Quantification of RyR1 pore radius was performed in HOLE and visualized in Excel (Figure S6). Quantification of FKBP and Nb9657 occupancies in cryo-EM maps was performed using OccuPy (Figure S4). For FKBP, occupancy was also estimated using 3D classification in cryoSPARC (Figure S5; Table S1). Real-space cross-correlation of lipid models with cryo-EM density was calculated using Phenix (Figure S8).